Elasto-Plastic Effects on Shape-Shifting Electron-Beam-Patterned Gel-Based Micro-Helices

Journal:	*Materials Horizons*
Manuscript ID	MH-COM-02-2024-000208.R1
Article Type:	Communication
Date Submitted by the Author:	19-Apr-2024
Complete List of Authors:	Wu, Xinpei; Stevens Institute of Technology, Dept. of Chemical Engineering and Materials Science Teng, Feiyue; Brookhaven National Laboratory, Center for Functional Nanomaterials Firlar, Emre; Rutgers The State University of New Jersey, Zhang, Teng; Syracuse University, Mechanical and Aerospace Engineering Libera, Matthew; Stevens Institute of Technology, Dept. of Chemical Engineering and Materials Science

COMMUNICATION

Elasto-Plastic Effects on Shape-Shifting Electron-Beam-Patterned Gel-Based Micro-Helices

Received 00th January 20xx,
Accepted 00th January 20xx

DOI: 10.1039/x0xx00000x

Xinpei Wu,[a] Feiyue Teng,[a,b] Emre Firlar,[c,d] Teng Zhang,[e] and Matthew Libera[a†]

Shape-shifting helical gels have been created by various routes, notably by photolithography. We explore electron-beam lithography as an alternative to prescribe microhelix formation in tethered patterns of pure poly(acrylic acid). Simulations indicate the nanoscale spatial distribution of deposited energy that drives the loss of acid groups and crosslinking. Upon exposure to buffer, a patterned line converts to a 3D helix whose cross section comprises a crosslinked and hydrophobic core surrounded by a high-swelling pH-responsive corona. Through-thickness asymmetries generate out-of-plane bending to drive helix formation. The relative core and corona fractions are determined by the electron dose which in turn controls the helical radius and pitch. Increasing pH substantially raises the swelling stress and the rod elongates plastically. The pitch concurrently changes from minimal to non-minimal. The in-plane asymmetry driving this change can be attributed to shear-band formation in the hydrophobic core. Subsequent pH cycling drives elastic cycling of the helical properties. These findings illustrate the effects of elastoplastic deformation on helical properties and elaborate unique attributes of electron lithography as an alternate means to create shape-shifting structures.

New Concepts: We develop a new variation of electron-beam lithography able to pattern shape-shifting gel-based structures, specifically microhelices. Other approaches to create helices have used photolithography or the macroscopic assembly of layered sheets. E-beam patterning opens a different variable space that includes maskless control over the nanoscale distribution of deposited energy that drives local radiation chemistry. In contrast to photolithography, focused electrons can pattern pure homopolymers. Here, we concentrate on poly(acrylic acid) (PAA). Since PAA is a weak polyelectrolyte, the swelling and, hence, the magnitude of the bending stresses that drive shape shifting can be controlled by pH. Key helical properties cycle elastically with periodic pH changes. However, above pK_a the stresses are sufficient to drive plastic deformation which introduces in-plane anisotropies that convert the helical pitch from minimal to non-minimal. Unlike the intentional prescribing of lateral anisotropies used by other patterning methods, our system dynamically changes the pitch by a process intrinsic to the shape shifting itself. More broadly, we can expect that e-beam patterning strategies can be applied to almost any homopolymer that is cross-linkable by electrons, including hydrophobic homopolymers or multilayer homopolymer films, most of which cannot be studied by photolithography.

1. Introduction

Shape-shifting structures can be generated by patterning bending and buckling stresses that direct a material to deform in response to stimuli such as a change in temperature or hydration. One specific shape-shifting structure is the helix. Helices are manifested in nature by plant tendrils, seashells, animal horns, and, at a very different length scale, secondary and tertiary molecular structures. Helical structures can exhibit many different sizes and mechanical properties and are of particular interest due to their ability to mimic muscle action.[1, 2]

Shape-shifting helices form due to differential stresses through the thickness of a material where

---

[a] *Dept. of Chemical Engineering & Materials Science, Stevens Institute of Technology, Hoboken, NJ USA.*
[b] *presently with the Brookhaven National Laboratory, Upton, NY.*
[c] *Rutgers CryoEM & Nanoimaging Facility and Institute for Quantitative Biomedicine, Rutgers University, Piscataway, NJ .*
[d] *presently with Bristol Myers Squibb, Molecular Structure & Design, Princeton, NJ*
[e] *Dept. of Mechanical and Aerospace Engineering, Syracuse University, Syracuse, NY USA*
† corresponding author: mlibera@stevens.edu.

Electronic Supplementary Information (ESI) available: Detailed materials & methods, local swelling model, additional experimental data including 3D renderings of confocal images. See DOI: 10.1039/x0xx00000x the thickness (h) is typically much smaller than the two lateral dimensions of width (w) and initial length (L_o). In the particular case of shape-shifting gels, one way to impose differential stresses involves the layering of materials with different swelling properties.[3-7] The bending mechanics are then akin to the classical problem of a bilayer strip.[8] This approach is particularly useful for creating structures on mm-to-cm length scales, since sheets of material can be mechanically cut, oriented, and bonded prior to swelling. A second way is to impose a gradient in the crosslink density.[9-13] Such structures have been created using photolithography where light adsorption creates an exposure gradient which is highest at the incident surface and decreases with depth into the material.

Here we explore electron-beam (e-beam) lithography as an alternate method to impose swelling gradients. Like photolithography, the basic concept of depth-dependent radiative dose follows a Beer's-law decay of intensity with depth.[14] There are important differences, however.[15] Notably, while the incident photon energy in photolithography is typically fixed, the incident electron energy can be easily changed. Consequently, e-beams offer substantial control of the depth over which energy is deposited. E-beam processes also do not require a mask, and the digital inputs can be easily changed to create different patterns. Furthermore, since the pattern consists of a defined array of points, e-beams allow for specific control of the lateral distribution of deposited energy both by varying the interpixel spacing between adjacent points, δ, and by varying the radiative point dose, D_p, delivered to each pixel.

Another significant distinction is that e-beams can pattern homopolymers. Inelastic energy transfer occurs over a continuous range of electron energies up to the incident energy. In addition to direct knock-on displacement, valence electron excitations and the decay of excited plasmons can create radicals that induce various radiation chemistries able to drive crosslinking and other reactions. These can occur in simple polymer systems including pure and fully saturated homopolymer hydrocarbons.

We show that focused electron irradiation can pattern shape-shifting helices from homopolymer films of pure poly(acrylic acid) (PAA). Asymmetric swelling drives out-of-plane bending when the patterned structures are immersed in aqueous buffers. The swelling can be controlled by δ and D_p. Since PAA is a weak polyelectrolyte with a pK_a of about 5.0,[16, 17] pH provides an external trigger that can dramatically change the magnitude of swelling and influence the helical properties. In addition to elastic effects that correlate with pH, we show that plastic deformation can occur. This plasticity creates in-plane asymmetries which irreversibly affect the helical properties, notably the helical pitch, which converts from minimal to non-minimal.

2. Results and Discussion

2.1 Shape-shifting helices by e-beam patterning

Shape-shifting lines were e-beam patterned in films spin cast onto single-crystal Si substrates from solutions of Cy3-labeled homopolymer PAA (M_w = 450 kDa) dissolved in methanol. The patterning used a focused electron beam digitally rastered at an interpixel spacing δ_x of 2 nm. Each pixel was irradiated using electrons with an incident energy E_o of 2 keV or 10 keV and a point dose D_p (e.g., 4 fC).

Electron irradiation drives a number of radiation chemistries in polymers, the net effect of which can be crosslinking as manifested by the classical case of polystyrene.[18] Notable among non-traditional resists is poly(ethylene glycol) (PEG). E-beam patterning crosslinks PEG and can graft the crosslinked structure to an underlying substrate to produce surface-patterned micro/nano-scale gels. Such patterned gels have been used to control the spatial interactions of proteins and cells with surfaces as well as mediate site-specific chemistries.[19-21] Thin films of PAA have similarly been shown to crosslink under electron irradiation to form surface-grafted pH-responsive nanogels.[22] In contrast to PEG which forms semicrystalline films, solvent-cast PAA is amorphous and possible effects of varying polycrystalline structure on the patterning are avoided.

The patterned structures can be surface tethered by leveraging the influence of electron energy on penetration depth. Monte Carlo (MC) simulations [23] (Fig. 1A) indicate that the penetration of 2 keV electrons in a solid PAA film is much less than that of 10 keV electrons. We thus used PAA films with a thickness (t_o) of $\geq 500\,nm$ so 2 keV patterning would drive radiation chemistry near the film surface. These regions were then coupled to the substrate (Si) by a so-called tethering pad created using 10 keV electrons (Fig. 1B). Details of the simulations are provided as Supplementary Information. After patterning, the sample was developed using 0.01 M phosphate buffer ($[Na^+]$ = 0.0148 M) at pH 3.0 or 7.4. Left behind was a patterned structure tethered at one end to the substrate but otherwise free to adopt an equilibrium shape (Fig. 1C) in buffer.

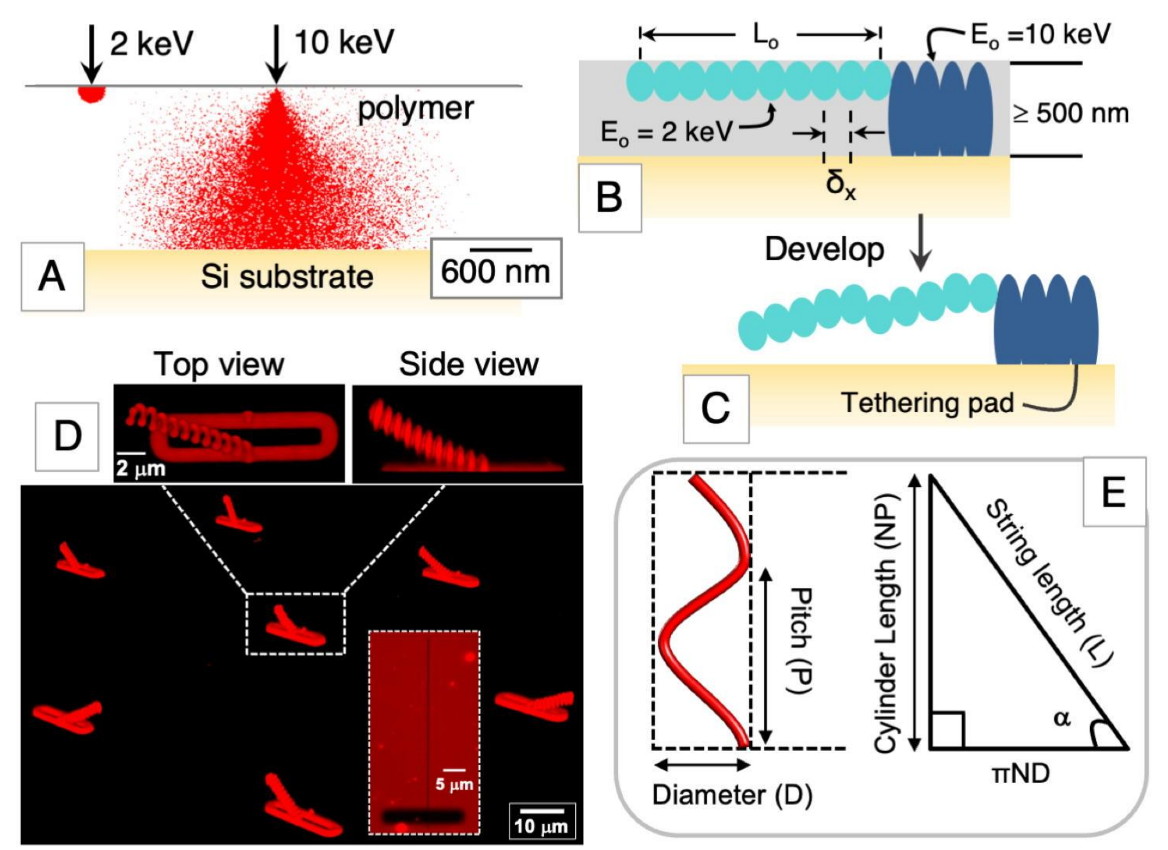

Figure. 1: (A) Monte Carlo simulation of electron trajectories shows the difference in penetration depth of 2 keV and 10 keV electrons. (B) A shape-shifting structure is patterned in the near-surface of a polymer film using 2 keV electrons. (C) Developing in a good solvent removes unexposed polymer while the shape-shifting structure remains tethered. (D) A confocal image of an array of hydrated PAA helical hydrogels (D_p= 4 fC) developed in 0.01 M phosphate buffer at pH 3.0. The inset shows a patterned PAA film (dry) prior to development. (E) Key parameters characterizing a helix where N is the number of helical repeats.

Fig. 1D shows one result where an array of straight lines (L_o = 60 μm) was patterned in a PAA homopolymer film (D_p = 4 fC), developed at pH 3.0, and then imaged while hydrated in pH 3.0 buffer. The lines transformed into helices. One such line prior to development is shown in the fluorescence image inset in Fig. 1D. The dark contrast that indicates the patterned line and tethering pad arises from electron-beam damage to the Cy3 groups. The key helical parameters are illustrated by Fig. 1E. The helix in Fig. 1D (top inset) is right-handed, its pitch (P) is 1.2 μm, its pitch angle α is 8.2°, its radius (R=D/2) is 1.3 μm, and its string length (L) is 65.6 μm.

2.2 Energy deposition generates swelling gradients

Shape shifting occurs upon hydration because of asymmetric swelling, which is determined by the spatial distribution of energy deposited by the electron beam. We modelled this distribution by repeating MC simulations of point irradiations spaced δ_x = 2 nm apart and summing the energy deposited in each voxel (8 nm^3). Fig. 2 presents 2-D sections of energy deposition perpendicular to the line direction ($\hat{x}$) far from the ends of the patterned line to avoid proximity effects. Fig. 2A represents the case where the point dose, D_p, is 40 fC. The simulation of Fig 2B was done identically except for the lower point dose of D_p = 4 fC.

We used a model of pH-dependent swelling [24] together with published G values [25, 26] to convert the energy per voxel into a corresponding measure of the swell ratio at each voxel (see Supplementary Information). A G value is defined as the number of chemical events that occur per 100 eV of deposited energy, and the published G values determine energy thresholds for crosslinking and for mass loss (via damage to pendant PAA acid groups). The model converts the number of crosslinks per molecule into a measure of the swell ratio, Q, where Q is the volume ratio of a hydrated voxel to the dry (as-irradiated) voxel. This model shows that patterning a line in a precursor film of PAA homopolymer generates a rod-like structure (Fig. 2C) with a non-swelling core, roughly hemispherical, surrounded by a high-swelling corona. Its cross section can be parsed into three general regions. Regions 1 and 2 correspond to the core. Here the model predicts Q = 1 (no swelling). In region 2 (light blue), the majority of monomers have lost their acid groups, and this region thus resembles a largely hydrophobic hydrocarbon. In region 1 (dark blue), the dose is high enough to heavily crosslink the material and damage the acid group on every monomer unit. Region 1 is thus hydrophobic with a modulus and yield strength greater than region 2. In contrast, the corona (region 3, green in Fig. 2) receives orders of magnitude less energy. It corresponds to a polyelectrolyte gel with a crosslink density that decreases nonlinearly radially away from the point of e-beam incidence.

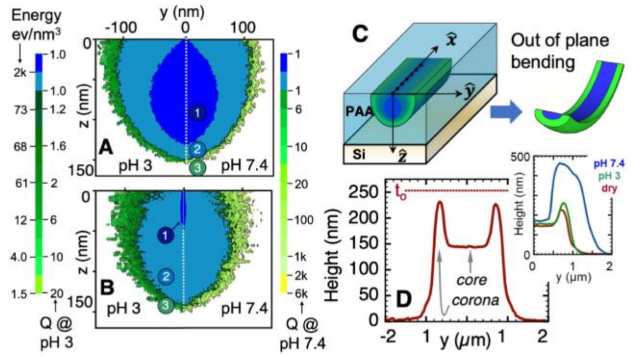

Figure 2: Monte Carlo simulations of energy deposition in the y-z plane for a line patterned along $\hat{x}$ (δ_x = 2 nm) with D_p = 40 fC (A) and 4 fC (B). Energy per voxel is converted into a volume swell ratio, Q, at pH 3 (left side) and pH 7.4 (right side). (C) Patterning a line along $\hat{x}$ produces a rod with a non-swelling core (blue) and a high-swelling corona (green). (D) AFM height profile across a dry line patterned (D_p = 40 fC) on a thin film (t_o = 253 nm). The inset shows partial profiles across the line when dry (red), at pH 3 (green), and at pH 7.4 (blue).

Atomic Force Microscopy (AFM) confirmed that the patterned line comprises a low-swelling core surrounded by a high-swelling and pH-dependent corona. To prevent helix formation, these measurements were done on thin films where the patterned line was grafted to the substrate. Fig. 2D shows a height profile across a line after development and drying. The central region (core) has a height of ~150 nm, which is substantially less than that of the dry precursor film (t_o = 253 nm) and indicates mass loss consistent with the radiation-driven CO/CO_2 release. There is less mass loss at the edges (corona). AFM also confirms that the core is low swelling (Fig. 2D inset). The core height increases only slightly when hydrated in either pH 3.0 or pH 7.4 buffer. In contrast, the corona swells under these same conditions and particularly so at the higher pH.

2.3 Helix formation

There is an extensive literature on helix formation.[27-29] In systems formed by photo-lithography or by manual bilayer fabrication,[3, 10, 12, 30-33] out-of-plane bending arises because of asymmetric deformation through the thickness ($\hat{z}$). In our case, the high-

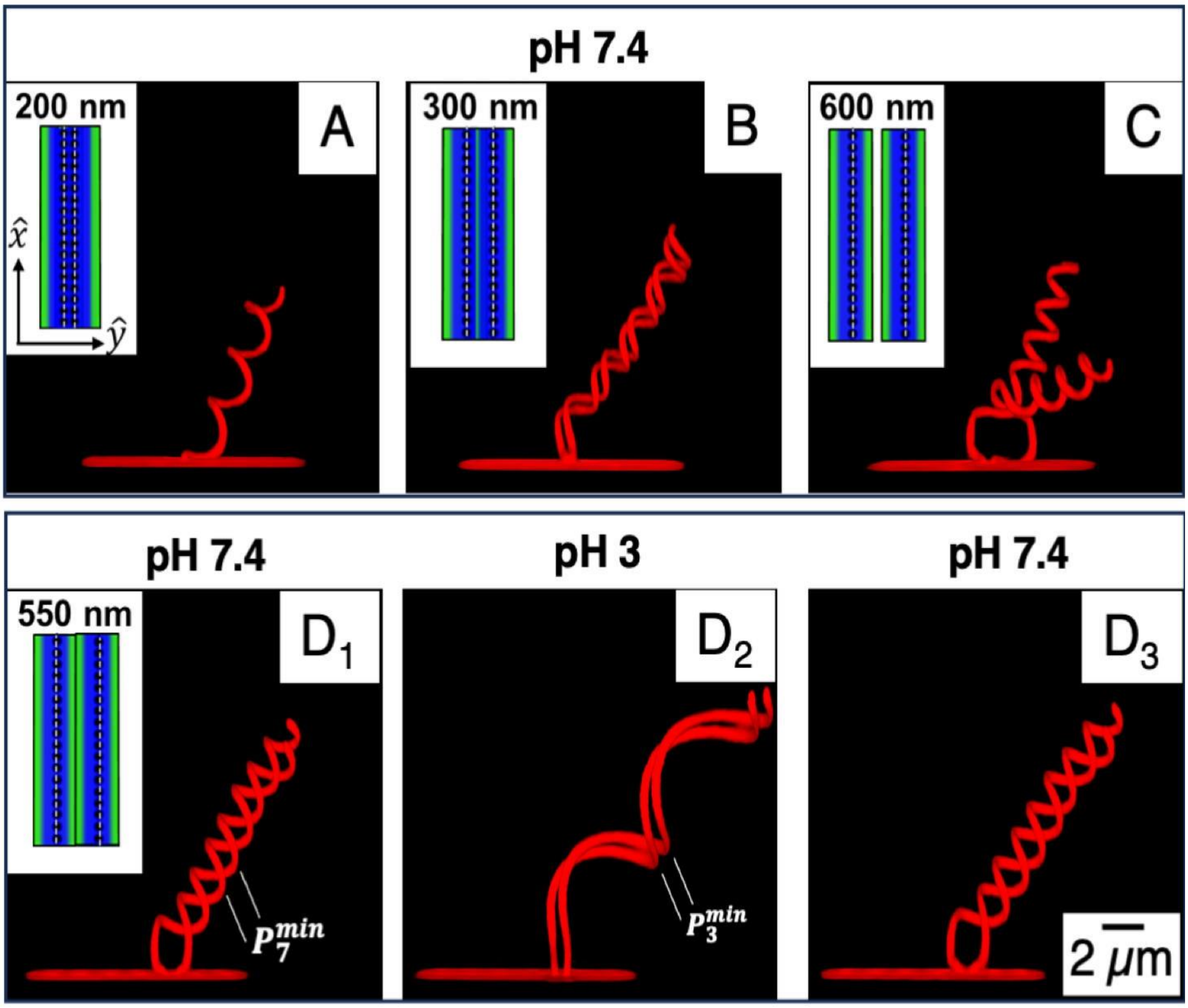

Figure 3: Patterned parallel lines separated by a distance Δy shape shift into single helices (A: Δy = 200 nm), double helices (B: Δy = 300 nm & D: Δy = 550 nm), and two independent helices (C: Δy = 600 nm) depending on the magnitude of Δy. All lines were patterned using D_p = 4 fC, δ_x = 2 nm, and L_o = 50 μm and developed in pH 7.4 buffer.

swelling corona forces the rod to deform out of the x-y plane.

Helix formation is understood in terms of minimizing the energies associated with out-of-plane bending and shear along the helical axis. A roll, which involves the formation of concentric layers where each subsequent layer has an incrementally larger radius, forms in the absence of shear.[34] Roll formation occurs in relatively wide ribbons. In contrast, the out-of-plane bending curvature in rods and narrow ribbons can remain constant if shear enables the self-avoiding condition where each consecutive turn just misses the preceding turn. This condition is met in our case of a narrow rod with out-of-plane bending due to the asymmetric swelling in $\hat{z}$.

In the absence of in-plane asymmetry, the elastic shear energy associated with the self-avoiding condition is minimized when subsequent helical turns are immediately adjacent to each other. In other words, the pitch is minimized. The helix in Fig. 1D is effectively minimal pitch even though there are gaps of dark contrast between adjacent turns. These gaps correspond to lightly crosslinked gel with a very low fluorophore concentration. To show this, identical lines (D_p = 4 fC; pH 7.4 developing buffer) were patterned parallel to each other and separated laterally by a distance Δy ranging from 50 nm to 1000 nm. For $\Delta y \leq 200$ nm, the two separate lines cannot be resolved (Fig. 3A). In contrast, double helices form for $300 \text{ nm} \leq \Delta y \leq 550$ nm (Figs. 3B & D). The two parallel lines trace similar helical paths offset from each other. For $\Delta y \geq 600$ nm (Fig. 3C), the two lines are independent. Their helical properties (pitch, radius, etc.) are similar, but their spatial trajectories are uncorrelated and their chirality is random.

These parallel-line experiments can be understood by considering the extent to which the electron interaction volumes overlap in the $\hat{y}$ direction (see Fig. 3 schematic insets). Figs. 3B and 3D show little/no fluorescent signal between the two lines, because the crosslinked corona material there is highly hydrated and the fluorophore concentration is extremely low. However, we confirmed that the two lines are physically connected by changing the pH from 7.4 (Fig. 3D$_1$) to 3.0 (Fig. 3D$_2$) and then back to 7.4 (Fig. 3D$_3$). The line separation decreased as expected when the crosslinked PAA deswelled at pH 3.0, and the larger separation was recovered when the pH was returned to 7.4. The fact that the lines do not separate indicates that they are physically (covalently) connected despite the contrast gap.

In addition to D_p = 4 fC, similar experiments were performed for D_p = 10 fC and 40 fC (See Figs. S2 and S3). We measured the size of the maximum contrast gap in each case, and we label it at pH 3.0 as P_3^{min} (Table 1). When referred to a patterned single line, these measurements can be used to differentiate between minimal and non-minimal-pitch helices. Since, for example, the pitch of the helix in the Fig. 1D top inset (D_p= 4 fC; pH = 3.0) is 1.2 µm and is less than 1.3 µm (Table 1), we can conclude that this is a minimal pitch helix. The very lightly crosslinked corona between subsequent turns of this helix touch each other and possibly compress the coronal gel there slightly.

Table 1 - Maximal contrast gaps give pitch thresholds for minimal pitch helices.

Point Dose (fC)	Center to center distance (µm); $[P_3^{min}]$.	Δy (nm)
	pH 3	
4	1.3	550
10	2.1	900
40	2.3	1200

An important basic issue raised by the parallel-line experiments centers on the electron range. The fact that the two lines become uncorrelated at separations of Δy > 500 nm indicates that the maximum lateral range of a 2 keV electron incident in PAA exceeds 250 nm. In contrast, our Monte Carlo simulations (Fig. 2A) suggest that this lateral range is only about 125 nm. We attribute the difference to two uncertainties in the simulations. First, the simulations only follow the electron trajectories until the electron energy falls to 5 eV. The remaining travel distance and how its energy is distributed along that final path to generate additional crosslinks is ignored. At the extreme periphery of the irradiated volume, for example, the network will terminate with polymer molecules attached by only one crosslink, and these are not accounted for by the model. Second is the uncertainty associated with the model used for the electron stopping power. While there is very good agreement between experiment and theory (Bethe model)[35] for electron energies of about 1 keV and more, stopping-power models for lower electron energies (E < ~200 eV), [36-40] overestimate the stopping power. In addition, there is also the experimental possibility of local substrate charging during electron irradiation, which could locally deflect the incident electron trajectory and thus increase the apparent electron range.

2.4 pH-controlled swelling

The pH controls the magnitude of swelling in the corona and thus influences the helical properties of single lines. The images in Fig. 4A, for example, follow the same two helices, patterned using different point doses, after they were developed in pH 3.0 buffer (D3 buffer), then immersed in pH 7.4 buffer, and then returned to pH 3.0 buffer. Figs. 4 B-D follow the longitudinal strain ($\epsilon = (L - L_0)/L_o$), the helical radius (R=D/2), and the pitch (P) during pH cycling. After the initial development step, these properties cycle elastically with each pH change. We estimate an upper bound of about 200-300 ms for these helices to shape-shift when the pH is changed (see Fig. S4), though the buffer change and subsequent image acquisition take much more time (tens of seconds). Fig. S5 shows pH cycling data for 30 cycles, at which point we stopped the experiment.

Fig. 4B shows the strain associated with lines (L_o = 100 µm) patterned using three different point doses as the lines were first developed in pH 3.0 (D3) buffer and then cycled between pH 7.4 and pH 3.0. When first developed, the string length in each case grows to produce the strain ϵ_{D3}. Subsequent exposure to pH 7.4 buffer increases the corona swell ratio by orders of magnitude, which further increases the longitudinal strain. Since the original strain is not recovered when the buffer is returned to pH 3.0, there is a plastic component (ϵ_{plas}). Subsequent cycling indicates that the elastic strain (ϵ_{elas}) is recoverable, but the plastic strain generated during the initial excursion to pH 7.4 remains. Fig. S6 shows that aging in pH 7.4 buffer for 5 days has little effect on the strain and pitch.

Strain data are summarized in Table 2. They display trends consistent with the relative mechanical properties of the patterned lines where the fraction of the most rigid region 1 material increases with dose (Fig. 4E). The 40 fC lines elongate the least while the 4 fC lines elongate the most with the 10 fC lines in between. While the pH change in itself has relatively little effect on the hydrophobic core (regions 1 & 2), it creates a substantially larger swelling force due to the polyelectrolyte gel in the corona (region 3). Fig. S6 indicates that aging in pH 7.4 buffer for 5 days provokes no recovery of the plastic deformation.

Table 2 - Average longitudinal strains (n = 5)

Point Dose (fC)	**pH 3.0 (D3)**	**pH 7.4**	**pH 3.0**	ϵ_{elas}	ϵ_{plas}
4	0.07	0.42	0.21	0.22	0.14
10	0.02	0.26	0.11	0.16	0.09
40	0.01	0.16	0.07	0.09	0.06

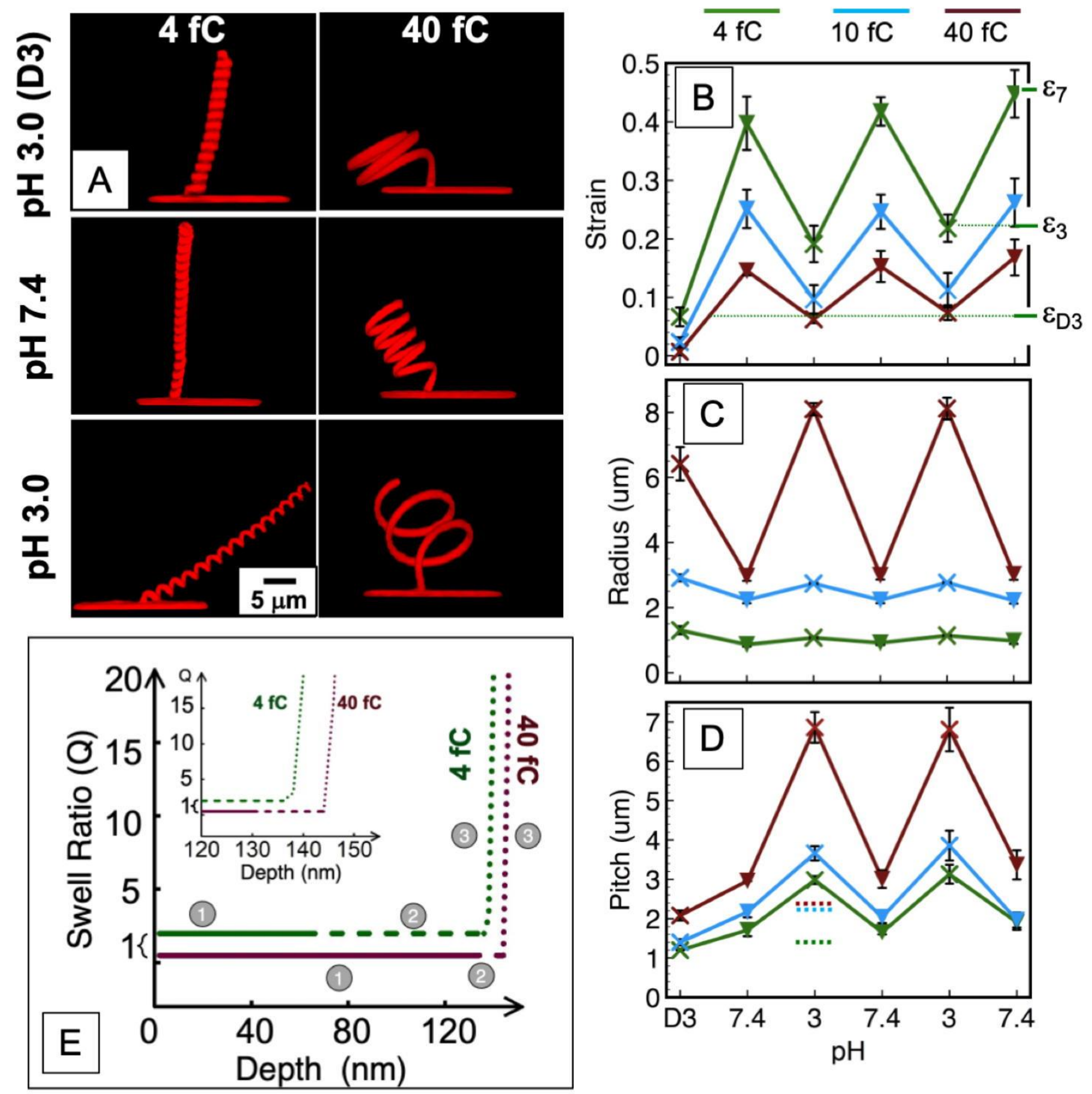

Figure 4: (A) Confocal images of hydrated helices formed from lines (L_o = 100 µm) patterned with D_p = 4 fC (left) and 40 fC (right) after developing in pH 3.0 buffer (top), then immersed in pH 7.4 buffer (middle), and then in pH 3.0 buffer (bottom). The helical properties as a function of pH (B, C, D). Each helix was developed in D3 buffer and then cycled between pH 7.4 and 3.0. The dotted lines in (D) indicate the maximum pitch at pH 3.0 for a minimal pitch helix. (E) Line profiles of swell ratio (pH 7.4) as a function of depth extracted from the MC simulations.

2.5 Plastic deformation creates a non-minimal pitch

Significantly, plastic deformation correlates with the formation of helices with a non-minimal pitch. This is indicated by the images and the strain data in Fig. 4. The double line experiments (Fig. 3) define threshold pitches that differentiate between minimal and non-minimal pitch helices (Table 1). The thresholds for pH 3.0 are indicated in Fig. 4D as color-coded dotted lines. For the three point doses the pitch at pH 3.0, after a prior excursion to pH 7.4, is greater than the corresponding threshold value. In other words, the plastic deformation induced by the pH change from D3 to 7.4 is preserved, as can be expected, when the pH is later changed from 7.4 back to 3.0, and this plastic deformation produces a non-minimal helical pitch.

2.6 Non-minimal pitch requires in-plane anisotropy

In helical systems where the pitch is non-minimal, there needs to be a mechanism to stabilize this extended conformation. Non-minimal pitch helices have been reported many times, and they are associated with some form of in-plane lateral anisotropy superimposed on the out-of-plane bending stress. Chen et al,[41] for example, embedded nitinol wires between latex sheets pre-strained in perpendicular directions and cut ribbons from the resulting bilayers at various angles relative the wire axis. Similarly, Kumacheva et al.[42] developed a hydrogel sheet with periodic stripes of different composition and different swelling properties with stripes oriented at angles relative to the long axis of the sheet. Other examples of lateral anisotropy include paper systems,[43] shape-shifting pasta,[44] and oriented inorganic bilayer thin films.[45]

The fact that lateral anisotropy can generate a non-minimal pitch helix is illustrated by the finite element (FE) simulation in Fig. 5. We conducted simulations of a core-shell composite rod with a semi-circular cross-section as a simplified model approximating the swelling profile in Figure 2. The rod geometry is shown in Figure 5A. Its length is 25 μm, its core diameter is 300 nm, and its coronal shell thickness is 60 nm. The mechanical anisotropy is assumed to be on the x-z plane with a major axis denoted as 1 and a minor axis as 2. E_i^c represents the elastic modulus of the core along the i=1 or 2 direction. Figure 5B illustrates the effect of in-plane anisotropy. When $E_1^c = E_2^c$, a minimal pitch helix is formed. Increasing the ${E_1^c}\big/{E_2^c}$ ratio to form an in-plane mechanical anisotropy generates a non-minimal pitch helix. Here we assumed the major axis is angled 45° with respect to the line direction of the rod consistent with possible shear band formation during plastic deformation (see below). We note, however, that other angles will generate non-minimal pitch helices if the anisotropic axes do not align with the geometric axes of the rod.

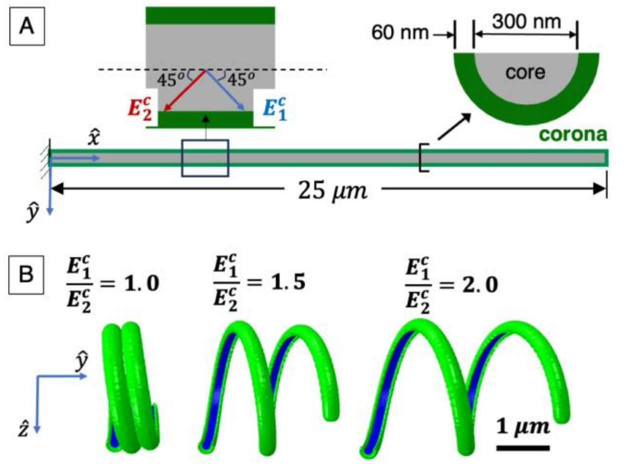

Figure 5: (A) The geometry of the simulated rod. (B) Snapshots of helices with different anisotropic material properties. Increasing the in-plane anisotropy increases the non-minimal pitch.

2.7 Anisotropy can be introduced by shear banding

We conjecture that plastic deformation creates a lateral anisotropy within our helical rods by shear banding. Despite that the core corresponds to a crosslinked homopolymer, this material, notably the softer region 2 material, can nevertheless plastically deform. The yielding and plastic deformation of amorphous polymers has been of longstanding interest to the scientific community.[46, 47] Post-yield plastic deformation in polymers typically occurs by crazing, shear banding, or a combination of the two.[48, 49] Modelling and experiments to understand such deformation remain an active research area.[50-52] Most relevant here is that shear bands tend to preferentially form under conditions of relatively high crosslinking[48, 53, 54] or spatial confinement.[55-57] Both conditions are present in region 2. Shear bands have distinct mechanical and structural properties compared to the surrounding material. Polymer segments between crosslinks can align along the direction of maximum shear stress. When these segments reach maximum extension, either the bands grow laterally or additional bands are nucleated elsewhere. Ward and Sweeney[46] argue that the preferred band angle is 54.7° away from the longitudinal axis. Within a band one can anticipate that the modulus will increase in the direction of the maximum shear stress due to the molecular alignment. Such a phenomenon would give rise to the lateral asymmetry in modulus simulated by Fig. 5 and can account for the development of non-minimal helices when macroscopic plastic deformation of the rods is observed.

2.8 Electron dose controls helical properties

Fig. 4 shows that the helical properties depend on the electron dose. Notably, the helical radius at a given pH is greater for lines patterned with D_p = 40 fC than those patterned with D_p = 4 fC (Fig. 4C), because the higher-dose lines have a greater resistance to the out-of-plane bending force. One illustration is given by the MC data (Fig. 2; pH 7.4), which are replotted in Fig. 4E as profiles of swell ratio as a function of depth (z). These simulations predict that the depth of the electron-polymer interaction is similar for two different point doses, consistent with the fact that the electron range is determined primarily by the incident electron energy. The cores, however, are strikingly different. The ratio of region 1 material (solid line) to region 2 material (dashed line) is substantially higher in the 40 fC case than in the 4 fC case.

We measured the helical radius across a range of point doses developed in pH 7.4 buffer (Fig. 6A) and then used these data to guide the patterning of variable-dose lines. Figs. 6B and 6C show confocal images of such lines that transformed into tendrils. The patterned lines comprised twenty 5 µm segments with each segment having a point dose 1 fC different from its nearest neighbors. The image data in Fig. 6 indicate that such patterning produces conical helices (tendrils) with a continuously varying radius. As expected, with dose increasing away from the tethering pad, the radius increases (Fig. 6B), and with dose decreasing away from the

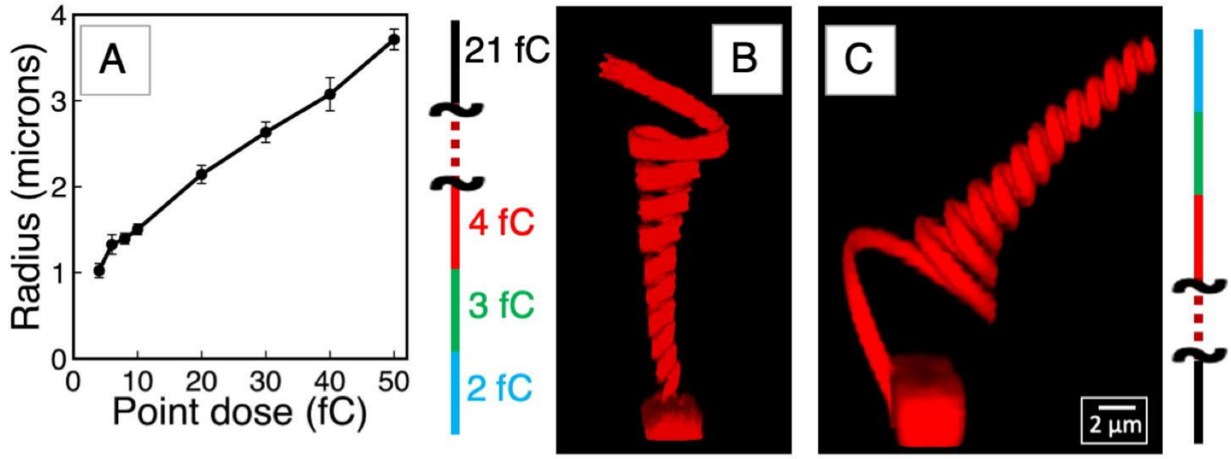

Figure 6: (A) The helical properties depend on incident point dose. Each data point and error bar correspond to the average and standard deviation of measurements from 5 different helices. (B & C) Tendrils were formed by patterning connected line segments each with incrementally different point doses developed and imaged in pH 7.4 buffer. The point dose increases (B) and decreases (C) by with increasing distance from the tethering pad. The total initial line length is L_0 = 100 µm.

tethering pad, the radius decreases (Fig. 6C). Not shown is the case where a segmented line was created first with an increasing and then with a decreasing point dose, which produced a tendril that first opened and then closed.

2.9 Patterned lateral anisotropy controls chirality

The chirality of single-line helices is random (Table 3). The helical properties (L, R, α, etc.) were furthermore independent of the chirality. Importantly, while patterning creates a clear depth-dependent swelling asymmetry that drives out-of-plane bending, the MC simulations (Fig. 2) indicate that there is no lateral asymmetry to dictate chirality. Whether the helix is left-handed or right-handed is left to chance. Fig. S7 shows that patterning a line at an angle of ± 45^o (rather than 90^o) relative to the tethering pad also has no effect on the chirality.

Similar random chirality occurred in double-stranded helices when the patterning conditions of each line were the same (Figs. 3B and D). We refer to these as symmetric double lines because of the identical patterning conditions for each line. In contrast, patterning parallel lines separated from each other laterally by a distance Δy where the exposure conditions for each line are different can provide complete control over the chirality. We refer to such patterns as asymmetric double lines.

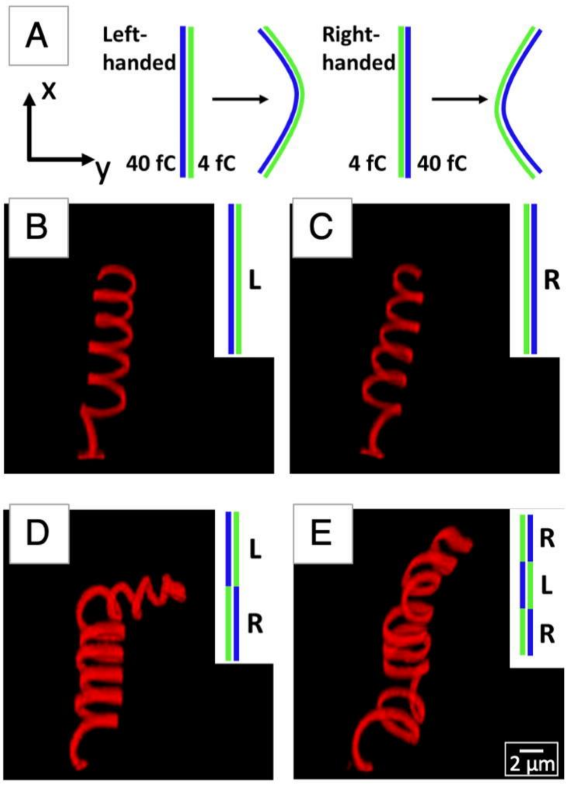

Figure 7: (A) Schematic asymmetric parallel lines with confocal images (pH 7.4) where one asymmetry generates a left-handed helix (B) and the inverted asymmetry generates a right-handed helix (C). A perversion is generated when the asymmetry is inverted once along the lines (D), and two perversions are generated when the asymmetry is inverted twice (E). L_o = 50 µm in (B) and (C), and L_o = 100 µm in (D) and (E).

We found a window of dose combinations and lateral offsets able to control chirality. Here we present results involving the asymmetric patterning of one line using 40 fC and a second parallel line offset by Δy = 200 nm using 4 fC. The geometry is illustrated by Fig. 7A, and example images are given in Figs 7B and 7C. In one case, the more rigid 40 fC line was patterned on the left side of the 4 fC line, and in the other case the 40 fC line was patterned on the right side. In contrast to single lines where the number of left-handed and right-handed helices observed is similar, asymmetric double lines exhibit only one chirality and that chirality inverts when the asymmetry is inverted (Table 3). The influence of the asymmetry can be attributed to the fact that the 4 fC line is less rigid than the 40 fC line and will

Table 3 - Chirality of patterned lines

Chirality	Single lines		Asymmetric double lines Left line/Right line	
	4 fC	40 fC	40/4 fC	4/40 fC
Left-handed	22	19	62	0
Right-handed	33	22	0	20

elongate more when exposed to solvent (see Table 2). This difference creates a bending moment much like the traditional bilayer strip but now with the bending moment in-plane rather than out-of-plane.

Because of the flexible patterning afforded by e-beam lithography, there are many variables which can be explored *vis a vis* chirality control. For example, in the case of asymmetric parallel lines, the asymmetry can be modulated along the length of the lines. Fig. 7D illustrates the effect of one such modulation where the asymmetry is inverted. This produces a perversion where the chirality inverts. In the case where the asymmetry is inverted twice (Fig. 7E) the resulting helix exhibits two perversions where the chirality starts as right-handed, inverts to left-handed, and then inverts back to right-handed.

Conclusions

We have used focused electrons to drive radiation-induced chemistry in films of pure poly(acrylic acid). 2 keV electrons crosslink PAA, and the spatial distribution of deposited energy creates asymmetric swelling gradients. Monte Carlo simulations of energy deposition coupled with a model of pH-dependent swelling indicate that patterning a one-dimensional line creates a three-dimensional rod structure comprising a low-swelling hydrophobic core along the rod axis surrounded by a high-swelling corona. This structure was confirmed by AFM. Exposing the patterns to low-ionic strength buffer released the rod from the unexposed PAA and enabled the rod to shape shift into a helix in response to swelling-induced out-of-plane bending.

Since PAA is a weak polyanion, cycling the pH above and below pK_a cycled the helical properties. Notably, initially increasing the pH to 7.4 from 3.0 produced a swelling pressure sufficient to drive both elastic and plastic deformation within the helices. The plasticity converted a helix initially manifesting a minimal pitch to one with a non-minimal pitch that is associated with an additional in-plane mechanical anisotropy. The formation of shear bands within the hydrophobic core can simultaneously account for both the plastic deformation and the concomitant development of a mechanical anisotropy due to strain-induced molecular alignment at an angle relative to the principal helical axis. In contrast to other approaches such as photolithography that rely on extrinsic patterning to impose a lateral anisotropy that generates non-minimal pitch helices, the anisotropic plastic deformation we observe is intrinsic to the material system and represents another controllable shape-shifting mechanism.

More generally, in the context of creating shape-shifting structures, e-beam patterning is almost entirely unexplored. It does, however, bring an array of processing variables – incident electron energy, radiative dose and spatial distribution of that dose – that can be exploited to make novel structures. E-beam approaches are maskless and provide considerable patterning flexibility. In addition to simple lines, this paper shows additional examples involving symmetric and asymmetric double lines which can produce double-stranded helices and chirality-controlled helices, respectively. Notably, without the need for initiators or complex chemistries, the space of potential polymer systems to study is large and unique. We have concentrated here on poly(acrylic acid), but the same ideas can be applied to almost any homopolymer system that preferentially crosslinks in response to electron irradiation, including hydrophobic polymers such as polystyrene or multilayer homopolymer systems.

Experimental section/methods

A detailed description of the materials and methods used in our experiments and models is provided as Supplementary Information.

Supplementary Information:

Available from the Wiley Online Library.

1. Materials and methods
2. Monte Carlo simulation
3. Modeling the swelling of e-beam patterned PAA
4. Upper bound on the pH-induced shape change of 200-300 msec.
5. Symmetric double line experiments at D_p = 10 fC and D_p = 40 fC.
6. pH cycling
7. Aging at pH 7.4
8. Effect of 45^{o} line orientation on chirality

Author Contributions

X.W., F.T., and M.L. conceived the idea of tethered shape-shifting structures via e-beam patterning. X.W. and M.L. designed the experiments. X.W. performed the experiments. E.F. and T.Z. performed Monte Carlo and finite element modelling, respectively. X.W. and M.L. did the primary writing. All authors participated in the review and editing. M.L. was responsible for funding acquisition and project administration.

Conflicts of interest

None.

Acknowledgements

This project was supported by the Army Research Office (W911NF2010277). The authors acknowledge the Office of Advanced Research Computing (OARC) at Rutgers University for providing computing resources for Monte Carlo simulations.

Notes and references

1. M. Kanik, S. Orguc, G. Varnavides, J. Kim, T. Benavides, D. Gonzalez, T. Akintilo, C. C. Tasan, A. P. Chandrakasan, Y. Fink and P. Anikeeva, *Science*, 2019, **365**, 145-150.
2. E. Acome, S. K. Mitchell, T. G. Morrissey, M. B. Emmett, C. Benjamin, M. King, M. Radakovitz and C. Keplinger, *Science*, 2018, **359**, 61-65.
3. A. S. Gladman, E. A. Matsumoto, R. G. Nuzzo, L. Mahadevan and J. A. Lewis, *Nat Mater*, 2016, **15**, 413-418.
4. T. van Manen, S. Janbaz and A. A. Zadpoor, *Materials Today*, 2018, **21**, 144-163.
5. O. Erol, A. Pantula, W. Liu and D. H. Gracias, *Advanced Materials Technologies*, 2019, **4**.
6. S. Armon, E. Efrati, R. Kupferman and E. Sharon, *Science*, 2011, **333**, 1726-1730.
7. Y. Liu, J. Genzer and M. D. Dickey, *Progress in Polymer Science*, 2016, **52**, 79-106.
8. S. Timoshenko, *J. Opt. Soc. Am.*, 1925, **11**, 233--255.
9. Z. Hu, X. Zhang and Y. Li, *Science*, 1995, **269**, 525-527.
10. J. Kim, J. A. Hanna, M. Byun, C. D. Santangelo and R. C. Hayward, *Science*, 2012, **335**, 1201-1205.
11. Y. Zhou, C. M. Duque, C. D. Santangelo and R. C. Hayward, *Advanced Functional Materials*, 2019, **29**.
12. C. N. Zhu, C. Y. Li, H. Wang, W. Hong, F. Huang, Q. Zheng and Z. L. Wu, *Adv Mater*, 2021, **33**, e2008057.
13. L. Huang, R. Jiang, J. Wu, J. Song, H. Bai, B. Li, Q. Zhao and T. Xie, *Adv Mater*, 2017, **29**.
14. T. Malis, S. C. Cheng and R. F. Egerton, *J. Electron Microsc. Tech.*, 1988, **8**, 193-200.
15. A. Singh, A. Shi and S. A. Claridge, *Chem. Commun.*, 2022, **58**, 13059-13070.
16. T. Swift, L. Swanson, M. Geoghegan and S. Rimmer, *Soft Matter*, 2016, **12**, 2542-2549.
17. X. Xiao, J. Ji, W. Zhou, S. Nanjia and M. Libera, *Macromolecules*, 2022, **55**, 1736-1746.
18. H. Y. Ku and L. C. Scala, *Journal of The Electrochemical Society*, 1969, **116**, 980.
19. K. L. Christman, E. Schopf, R. M. Broyer, R. C. Li, Y. Chen and H. D. Maynard, *J. Am. Chem. Soc.*, 2009, **131**, 521-527.
20. C. M. Kolodziej and H. D. Maynard, *Chem. Mater.*, 2012, **24**, 774-780.
21. Y. Wang, E. Firlar, X. Dai and M. Libera, *J Polym Sci Part B*, 2013, **51**, 1543-1554.
22. I. Saaem and J. Tian, *Advanced Materials*, 2007, **19**, 4268-4271.
23. D. C. Joy, *Monte Carlo Modeling for Electron Microscopy and Microanalysis*, Oxford University Press, New York, 1995.
24. D. Jia and M. Muthukumar, *Gels*, 2021, **7**.

25. C. L. Moad and D. J. Winzor, *Progress in Polymer Science*, 1998, DOI: 10.1016/s0079-6700(97)00041-5.
26. D. J. T. Hill, J. H. O'Donnell, C. L. Winzor and D. J. Winzor, *Polymer*, 1990, **31**, 538-542.
27. Z. Chen, C. Majidi, D. J. Srolovitz and M. Haataja, *Applied Physics Letters*, 2011, **98**, 011906.
28. N. Chouaieb, A. Goriely and J. H. Maddocks, *Proceedings of the National Academy of Sciences*, 2006, **103**, 9398-9403.
29. G. M. Spinks, *Adv Mater*, 2020, **32**, e1904093.
30. A. Mourran, H. Zhang, R. Vinokur and M. Moller, *Adv Mater*, 2017, **29**.
31. Z. L. Wu, M. Moshe, J. Greener, H. Therien-Aubin, Z. Nie, E. Sharon and E. Kumacheva, *Nat Commun*, 2013, **4**, 1586.
32. X. Liu, M. Gao, J. Chen, S. Guo, W. Zhu, L. Bai, W. Zhai, H. Du, H. Wu, C. Yan, Y. Shi, J. Gu, H. J. Qi and K. Zhou, *Advanced Functional Materials*, 2022, DOI: 10.1002/adfm.202203323.
33. Y. Dong, A. N. Ramey-Ward and K. Salaita, *Adv Mater*, 2021, **33**, e2006600.
34. J. Huang, J. Liu, B. Kroll, K. Bertoldi and D. R. Clarke, *Soft Matter*, 2012, **8**, 6291-6300.
35. H. Bethe, *Annalen der Physik*, 1930, **397**, 325-400.
36. D. C. Joy and S. Luo, *Scanning*, 1989, **11**.
37. D. C. Joy, S. Luo, R. Gauvin, P. Hovington and N. Evans, *Scanning Microsc.*, 1996, **10**, 653-666.
38. D. Tahir, N. H. Sari, Suarga and Yulianti, *Appl. Radiat. Isot.*, 2015, **95**, 59-62.
39. G. Wilson and J. R. Dennison, *IEEE Trans Plasma Sci*, 2012, **40**, 291-297.
40. T. Zhenyu and H. Yancai, *Scanning*, 2002, **24**, 46-51.
41. X. Yu, L. Zhang, N. Hu, H. Grover, S. Huang, D. Wang and Z. Chen, *Applied Physics Letters*, 2017, **110**.
42. Z. L. Wu, M. Moshe, J. Greener, H. Therien-Aubin, Z. Nie, E. Sharon and E. Kumacheva, *Nat. Commun.*, 2013, **4**.
43. Y. Forterre and J. Dumais, *Science*, 2011, **333**, 1715-1716.
44. Y. Tao, Y. C. Lee, H. Liu, X. Zhang, J. Cui, C. Mondoa, M. Babaei, J. Santillan, G. Wang, D. Luo, D. Liu, H. Yang, Y. Do, L. Sun, W. Wang, T. Zhang and L. Yao, *Sci. Adv.*, 2021, **7**.
45. M. Huang, C. Boons, M. Roberts, D. E. Savage, M. G. Lagally, N. Shaji, H. Qin, R. Blick, J. A. Nairn and F. Liu, *Advanced Materials*, 2005, **17**, 2860-2864.
46. I. M. Ward and J. Sweeney, *Mechanical Properties of Solid Polymers*, Wiley, United Kingdom, 3rd edn., 2013.
47. R. N. Haward, *The Physics of Glassy Polymers*, Wiley, New York, 1973.
48. A. M. Donald and E. J. Kramer, *Journal of Materials Science*, 1982, **17**, 1871-1879.
49. J. C. M. Li, *Polym Eng Sci*, 1984, **24**, 750-760.
50. T. Lan, T. Shao, Y. Zhang, Y. Zhang, J. Zhu, Y. Jiang and P. Wu, *Eur J Mech A Solids*, 2023, DOI: 10.1016/j.euromechsol.2023.105015.
51. W. Shan, K. Xiao and E. L. Thomas, *Macromolecules*, 2022, **55**, 9594-9600.
52. W. Tang, D. Li, Y. Peng and P. Wu, *Polymer*, 2022, **255**.
53. C. G'Sell, D. Jacques and J. P. Favre, *Journal of Materials Science*, 1990, **25**, 2004-2010.
54. C. S. Henkee and E. J. Kramer, *J Polym Sci Part B*, 1996, **34**, 2825-2841.
55. R. K. Bay, S. Shimomura, Y. Liu, M. Ilton and A. J. Crosby, *Macromolecules*, 2018, **51**, 3647-3653.
56. R. J. S. Ivancic and R. A. Riggleman, *Soft Matter*, 2019, **15**, 4548-4561.
57. N. R. Velez, F. I. Allen, M. A. Jones, S. Govindjee, G. F. Meyers and A. M. Minor, *Macromolecules*, 2020, **53**, 8650-8662.